

Reconstruction of time-averaged 3D pressure fields in the wake of an Ahmed body with pressure from PIV

M. Ladwig¹, T. Gericke², S. Hüttig², R. Lindken¹

¹Bochum University of Applied Sciences, Institute of Thermo- and Fluid Mechanics, Bochum, Germany

²Volkswagen AG, Wolfsburg, Germany

* Correspondent author: marc.ladwig@hs-bochum.de

Keywords: Time-averaged pressure, Pressure from PIV, External car aerodynamics, Wake flow, Stereoscopic PIV, 3D-PTV

ABSTRACT

In this contribution we present and compare time-averaged pressure fields reconstructed from scanned stereoscopic 2D3C-PIV data and volumetric 3D-PTV data (Shake-The-Box) with classic pointwise surface pressure tap measurements. Measurements were conducted in the near-wake region of an one-quarter scaled Ahmed body (Ahmed 1984) with 25° slant angle at height-based Reynolds numbers of $Re = 5.06 \cdot 10^4$ and $1.13 \cdot 10^5$, respectively, i.e. free-stream velocities of 10.5 ms^{-1} and 23.5 ms^{-1} . The measurements are a continuation of previous measurements (Gericke et al. 2023, Ladwig et al. 2023) with focus on a more complex flow topology, particularly the flow structure in the wake. Measurements were conducted in a low-speed wind tunnel of Göttinger design with semi-closed test section at Bochum University of Applied Sciences. The investigated flow field in the near wake region is predominantly characterised by a strongly three-dimensional flow field based on a mutually influencing vortex system in the wake, which challenges the utilized pressure reconstruction algorithm based on the Reynolds-averaged Navier-Stokes equations. The present study addresses challenges in pressure reconstruction, due to the presence of highly transient rotational and shearing flow, in the context of a practical application. The results show good agreement between reconstructed PIV/PTV-based pressure fields and reference pressure measurements using classic wall pressure measurements. The global characteristics of the pressure distributions are correctly reproduced. The agreement is particularly good in areas of unidirectional flow and local smaller velocity gradients. In shear zones as well as separation and e.g., recirculation areas, larger deviations are clearly visible, as the velocity gradients present near the surface are not sufficiently captured at all.

1. Introduction

The experimental determination of planar and volumetric pressure distributions in aerodynamic studies is still a challenge and an important measurement tool. Particularly when, in addition to time-resolved data, increased demands are set on the spatial resolution of the pressure fields, classic pointwise pressure measurements using pressure boreholes and probes quickly reach their limits due to a lack of applicability, practicability and the outweighing inherently low spatial resolution. The reconstruction of corresponding pressure fields from velocity data based on 2D3C stereoscopic Particle Image Velocimetry (PIV) or 3D3C Particle Tracking Velocimetry (PTV) can

contribute to a better experimental implementation of pressure measurements, as the non-intrusive character of laser-based PIV and PTV methods signifies that cost-intensive and intrusive model preparations for, e.g. pressure taps, could be omitted. Further the pressure estimation as a post processing operation itself usually does not require additional setup components, beyond the existing systems used for estimation of velocity fields. Furthermore the implementation of pointwise pressure measurements is not always possible, e.g. due to limited space or a complex thin model structure (e.g., Jux et al. 2019). However since the velocity information is a measured quantity by PIV or PTV, errors must be considered since the reconstructed pressure is a derived quantity (e.g. van Oudheusden 2007, van Gent 2017). Planar and volumetric laser-optical measurement techniques like PIV and PTV provide velocity data with sufficient spatial resolution and dynamic range to offer a basis for pressure field estimation. A variety of methods for estimating pressure data from velocity data appeared in recent years, e.g., van Oudheusden 2013. Depending on the nature of available velocity data and the focus of the investigation, the four main approaches can be separated into Reynolds-averaging- (van Oudheusden et al. 2007), Eulerian- (de Kat and van Oudheusden 2012), pseudo-Lagrangian- (de Kat and van Oudheusden 2012) and the Taylor hypothesis approach (de Kat and Ganapathisubramani 2012). In this study a $\frac{1}{4}$ model of the Ahmed reference body (Ahmed 1984) was chosen for pressure reconstruction, due to its general acceptance for experimental and numeric studies and the steadily growing number of investigations, e.g. (Lienhardt and Becker 2003, Minguez et al. 2008, Sellappan et al. 2018)

The determination of pressure fields from 2D3C PIV and PTV data in this contribution is based on the Reynolds-averaging approach, using the Reynolds-averaged Navier-Stokes equations for pressure reconstruction as described in more detail, e.g., in van Oudheusden (2013). Under the assumption of an incompressible fluid in the subsonic flow regime with constant density, the momentum equation can be written in the form:

$$\frac{\partial \mathbf{u}}{\partial t} + (\mathbf{u} \cdot \nabla) \mathbf{u} - \nu \nabla^2 \mathbf{u} = \frac{1}{\rho} \nabla p + \mathbf{g} \quad (1)$$

with ν being the kinematic viscosity, ρ the fluid density and \mathbf{g} a vector of body forces which are neglectable in the present study, Eq. (1) can be rewritten further as:

$$\nabla p = -\rho \left(\frac{\partial \mathbf{u}}{\partial t} + (\mathbf{u} \cdot \nabla) \mathbf{u} \right) + \nu \rho \nabla^2 \mathbf{u} \quad (2)$$

In this study no time-resolved data is available, the pressure gradients therefore must be calculated from the local ensemble averaged velocity gradients. Following the Reynolds-averaging approach, equation (2) can be rewritten as:

$$\nabla \bar{p} = -\rho \left((\bar{\mathbf{u}} \cdot \nabla) \bar{\mathbf{u}} + \nabla \cdot \overline{\mathbf{u}'\mathbf{u}'} - \nu \rho \nabla^2 \bar{\mathbf{u}} \right) \quad (3)$$

The pressure field is then calculated by spatial integration of equation (3) by solving the related Poisson equation (4).

$$\nabla^2 \bar{p} = \nabla \cdot \left[-\rho \left((\bar{\mathbf{u}} \cdot \nabla) \bar{\mathbf{u}} + \nabla \cdot \overline{\mathbf{u}'\mathbf{u}'} - \nu \rho \nabla^2 \bar{\mathbf{u}} \right) \right] \quad (4)$$

To fully close the mathematical problem, additional boundary conditions must be provided in terms of Dirichlet boundary conditions (e.g., measured pressure values) or Neumann boundary conditions (e.g., pressure gradients) on the integration domain.

2. Experimental Setup

2.1 Wind tunnel facility

The measurements presented in this study were conducted in a low-speed closed-loop wind tunnel with 0.5 m nozzle outlet diameter and 1.5 m test section length at Bochum University of Applied Sciences, which is of a Göttinger design. A schematic overview is given in figure 2. Classic pointwise surface pressure, stereoscopic PIV and Shake-The-Box measurements were conducted at free-stream velocities of 10.5 ms^{-1} and 23.5 ms^{-1} leading to Reynolds numbers based on the undisturbed mean velocity and the height of the $\frac{1}{4}$ scaled Ahmed body of $Re = 5.06 \cdot 10^4$ and $Re = 1.13 \cdot 10^5$, respectively. Equal flow conditions were aimed during PIV and PTV measurements to ensure comparability of the results. The wind tunnel facility is driven by an axial fan ($Q_{\text{max}} = 8.5 \text{ m}^3/\text{s}$) which is powered by a 11 kW speed-controlled induction motor ($n_{\text{max}} = 1.450 \text{ min}^{-1}$). The flow within the test section is conditioned by an upstream positioned contraction nozzle (contraction ratio 1:5) which has an optimized contour for measurements in the subsonic range (Boerger 1973).

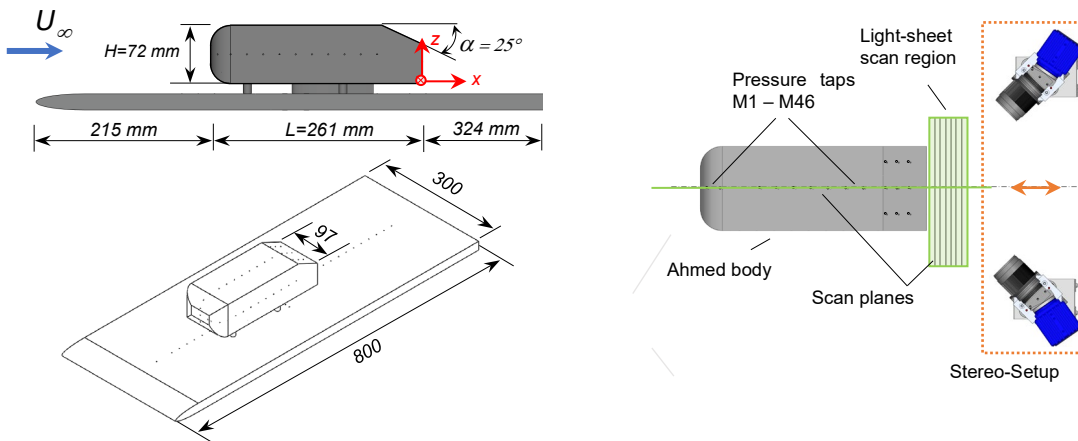


Figure 1: Geometric dimensions of the $\frac{1}{4}$ scaled Ahmed body model (left), and the schematic representation of the Stereo-PIV scan positions in the streamwise symmetry plane $y/H = 0$ and in spanwise direction in the wake behind the model. (right).

The ensemble averaged turbulence intensity in the middle of the test section was estimated from the variance of the velocity fluctuations in previous PIV measurements to $Tu = 3.5 \%$. This value is significantly larger compared to the minimum reachable turbulence level ($< 1\%$) of the wind tunnel, because small scale flow screens upstream the nozzle had to be removed to support 'Shake

the Box' (3D-PTV) measurements. This was necessary for the prevention of constipation of the turbulence screens by helium filled soap bubbles (HFSB) and as a consequence an increased flow resistance. For comparability of the results PTV and PIV measurements are both performed without turbulence screens. The remaining flow straightener arrangement has a rectangular mesh size of 20 mm. Surface pressure measurements were performed at 83 pressure taps located on the flat plate (37 boreholes, Indices P1 – P37) and the Ahmed body (46 boreholes, Indices M1 – M46), simultaneously. The wall static pressure signals were measured via a piezoresistive 96-channel pressure acquisition system (Scanivalve DSA3217) through sharp edged boreholes with 0.8 mm diameter. Time series of 2 minutes were sampled at 10 Hz and exploited to calculate the temporal mean pressure for further estimates of the local reference pressure coefficients. In this study only nine pressure values (see table 2) on the rear-surface of the Ahmed body were used for comparison. In addition, for reasons of reproducibility, pressure measurements were done three times. The pressure measurement results are flanked by error bars (see e.g. figure 8). During PIV measurements, the pressure taps on the Ahmed Body were taped by matt black tape (Sanjotape, matt black 4119), to minimize direct laser reflections from boreholes. The taps were not covered during the PTV measurements. The one-quarter scaled Ahmed body model is mounted on a flat plate with an elliptical leading edge (6:1) with stream- and spanwise dimension of 800 mm in length x 300 mm in width. A NACA 0020 airfoil is placed between the plate top surface and the Ahmed body to cover and guide the pressure tubes and to minimize flow separation from pressure tubes in the transition area between body and plate. The leading edge is located 200 mm behind the wind tunnel nozzle outlet. Furthermore, the Ahmed body is placed 215 mm downstream the leading edge.

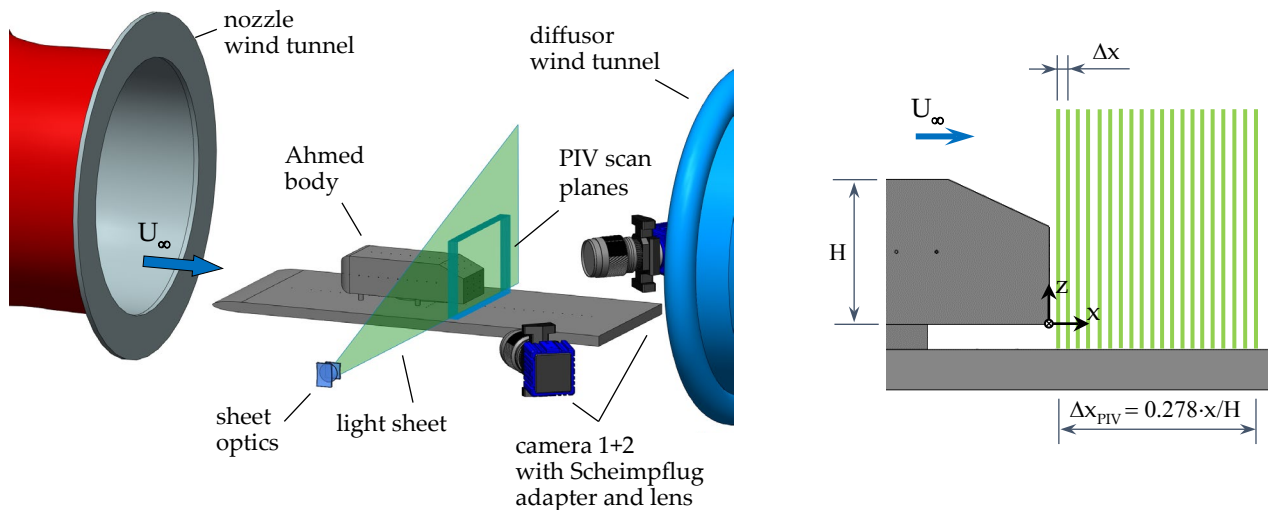


Figure 2: Wind tunnel setup used for stereoscopic PIV measurements in the near wake region (left). Base coordinate system and reference position of Stereo-PIV scan planes, Δx : distance between scan planes, Δx_{PIV} : total length of scan region in streamwise direction (right). Flow direction is from left to right.

2.3 Stereoscopic PIV setup

The stereoscopic PIV setup in this contribution (see figure 2) consists of two CMOS cameras (2560 × 2160 pixels, 16 bit, LaVision Imager sCMOS) in combination with macro lenses (Nikon Nikkor, T2.8/f = 60 mm) equipped with Scheimpflug adapters. An incidence angle between the cameras was chosen to 90°, which represents a compromise due to space constraints inside the test section. The Scheimpflug angle of both cameras was adjusted to comply the Scheimpflug condition (Prasad 2000, Westerweel and van Oord 2000, Willert 1997). The lens aperture was adjusted to $f\# = 4.0$. DEHS droplets were used as tracer particles (mean size $\sim 1 \mu\text{m}$), which were illuminated by a double-pulse Nd: YAG laser (Quantel Evergreen 200, repetition rate 15 Hz, 200 mJ) at a light wavelength of 532 nm. Particles were injected behind the collection diffuser between the first and second deflection corner of the wind tunnel. The laser beam was guided through a moveable laser guiding arm mounted an an automatized traversing system (Isel, LES 5), followed by a light sheet optic with diverging lens ($f = -20 \text{ mm}$) which forms the planar light sheet. The light sheet thickness was set to approximately 1.5 mm. A suitable seeding concentration and distribution in the test section was iteratively adjusted to maintain a mean particle image density of $N_i > 10$ to ensure a valid detection probability and a suitable signal to noise ratio (Adrian and Westerweel 2011). The timing between image acquisition of double frames from both cameras and pulsed illumination is synchronised by a timing unit (PTU X, LaVision). The main experimental parameters are listed in table 1.

Table 1: Experimental parameters

		Setup I (Stereo-PIV)	Setup II (PTV)
field of view	FOV	245 mm × 150 mm	volumetric
vector spacing	in-plane	$\Delta y = \Delta z = 0.62 \text{ mm}$	3.45 mm
	out-of-plane	$\Delta x = 1 \text{ mm}$	
pixel number	$N_x \times N_y$	2560 × 2160 px	1920 × 1280 px
pixel size		$6.5 \mu\text{m} \times 6.5 \mu\text{m}$	$4.8 \mu\text{m} \times 4.8 \mu\text{m}$
camera		Imager sCMOS, LaVision	CMOS, LaVision
lense		Nikon Nikkor $f = 60 \text{ mm}$	$f = 12 \text{ mm}$
f-number	$f\#$	4.0	6.0
light-sheet thickness	Δz_0	1.5 mm	volumetric
recording frequency	f_s	15 Hz	50 Hz
pulse separation	Δt	$45 \mu\text{s}^1$ ($20 \mu\text{s}$) ²	$150 \mu\text{s}^1$ ($82 \mu\text{s}$) ²
laser wavelength	λ	532 nm	
tracer material		DEHS	HFSB
mean tracer size	d_p	$1 \mu\text{m}$	$300 \mu\text{m}$
dynamic spatial range	DSR	53	188
dynamic velocity range	DVR	275	57

¹ Δt at $U_\infty = 10 \text{ ms}^{-1}$, ² Δt at $U_\infty = 23.5 \text{ ms}^{-1}$

A two-level three-dimensional calibration plate, mounted on optomechanical components, was used for the geometric calibration. The calibration plate (LaVision, Type 22) consists of 169 dots per plane with a center-to-center spacing of 15 mm, a dot diameter of 3.2 mm and a level displacement of 3 mm. After the geometric calibration a planar self-calibration (Wieneke 2005) with the use of experimental data in DaVis 10.2.1 is performed. A pinhole model is used for image mapping, which is fitted to the setup based on the previous geometric calibration. For scanning purposes over a three-dimensional region of interest, the stereoscopic setup is traversable in two axes. Acquisition and processing of single exposed double frames is done within Davis 10.2. A number of 3.000 double frame pairs were recorded at each scan position. The calibration routine, projection of the oblique recorded double frame recordings and the stereoscopic reconstruction in Davis is based on the methodology described in Wieneke (2005), which proposes an additional implemented 'self-calibration' routine to correct misalignments between the light sheet plane and the measurement plane, it was iteratively applied in this study. Figure 2 shows the scan position of scanned planes in y-z direction in the wake. In summary 20 scan planes were addressed by the PIV-setup, with an equidistant spacing of $\Delta y = 1$ mm between scan planes. A volumetric region ranging from $x/H = 0.0347$ to $x/H = 0.2986$ in streamwise direction and $y/H = -1.5$ to $y/H = 1.5$ in spanwise direction, is covered by present PIV measurements. Repositioning in streamwise direction between scan planes was realized by shifting the cameras and the light sheet optics with the tethered laser guiding arm collectively by means of a controllable linear unit with a mean traversing accuracy of $20 \mu\text{m}$ in both directions.

2.2 Tomographic 3D3C-PTV setup

Corresponding 3D-PTV measurements were done by means of a coaxial volumetric velocimeter (LaVision Mini-Shaker), which exhibits four CMOS-Cameras with a frame rate of 100 Hz at full resolution of 1920×1280 pixels with macro planar lenses (f-number = 6, $f\# = 12$ mm).

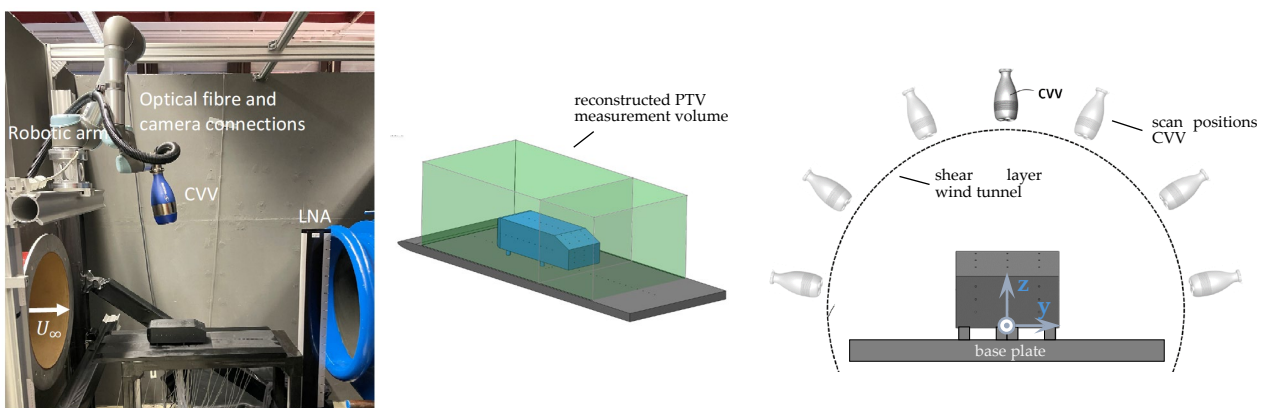


Figure 3: PTV (Shake-The-Box) setup consisting of a coaxial volumetric velocimeter (CVV) (Mini Shaker Aero, LaVision) mounted on a robotic arm within the wind tunnel test section at Bochum University of Applied Sciences and linear nozzle array (LNA) for helium filled soap bubble (HFBS) injection (left). Schematic sketch of CVV scan positions in y-z plane, (scan positions in x-direction are not shown) (right), and the green reconstructed PTV measurement volume (middle, only partially shown for clarity).

In addition, the Mini Shaker incorporates lenses for the volumetric expansion of the laser beam. Camera pixel size is 4.8 μm . The camera focal point was set 430 mm away from the center of the front cap. Illumination is provided by a Litron Bernoulli Nd:YAG laser with an output energy of 50 mJ per pulse at a wavelength of 532 nm and a frequency of 100 Hz. The laser is connected to the head of the MiniShaker via a coupler and an optical fiber. A typical volumetric field of view starts at $z = 360$ mm with a FOV of 150×70 mm² which extends to 230×130 mm² at $z = 540$ mm. Synchronization between laser and cameras is assured by a synchronization unit (PTU X, LaVision). The position and orientation of the MiniShaker head is controlled by a robotic arm (UR5, Universal Robots) with six degrees of freedom. Position repeatability is stated by the manufacturer as ± 0.1 mm. The robot is installed at one base position for all measurements (figure 2). Helium-filled soap bubbles (HFSB) were used as tracer particles with a mean diameter of 300 μm . The seeding system consists of a fluid supply unit (FSU), one Linear Nozzle Array (LNA) and a power supply unit (included in FSU). HFSBs are generated by nozzles implemented in an aerodynamically optimized NACA 0016 profile. The LNA was installed directly at the end of the test section in front of the collection diffusor (see figure 3, left). From 20 nozzles only 15 were positioned in the flow. Each nozzle generates up to 40.000 soap bubbles per second. Particle images are analyzed by means of the Shake-The-Box algorithm (Schanz et al. 2016) implemented in Davis 10. Every sub-volume of the $Re = 5.06 \cdot 10^4$ case contains approximately 3.8 million particle tracks. For the $Re = 1.13 \cdot 10^5$ case every sub-volume contains approximately 3.0 million particle tracks. After particle tracking, the sub-volumes are merged together and time-averaged velocities on a three-dimensional grid are calculated using binning with a bin size of $64 \times 64 \times 64$ voxel at 75% overlap- resulting in a 16 voxel (3.46 mm) vector spacing. Further details regarding the PTV-setup can be found in Gericke et al. 2023. A number of 4.000 double frames from each of the four cameras was recorded.

Based on the experimental setup used for PIV, PTV and pressure measurements, complementary CFD calculations were performed for both Reynolds number cases with OpenFOAM, which are shown in the results section. A one-equation delayed detached eddy model (IDDES) was chosen for turbulence modeling. Computations were performed for 2 seconds with a time step of $2 \cdot 10^{-5}$ seconds. The computational grid consists of 156 million cells, boundary layers around the Ahmed Body were resolved in terms of a low-Reynolds approach with $y^+ < 1$. But a detailed analysis of the CFD results is beyond the scope of this contribution.

2.3 Data processing of PIV datasets

The image pre-processing of raw images first consisted of a subtraction of the sliding intensity minimum for each pixel position combined with a spatial high-pass filter to effectively eliminate remaining reflections (see figure 4).

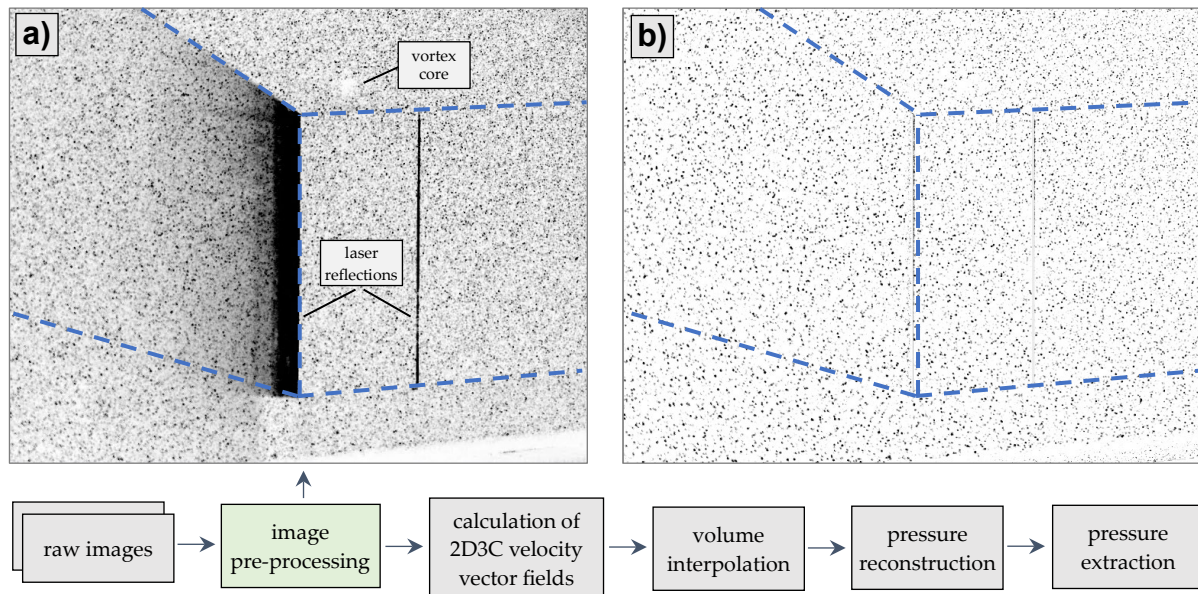


Figure 4: Image pre-processing of raw double frames acquire by stereo-PIV cam 1, focused on y - z plane at $x/H = 0.0486$ (3.5 mm behind the Ahmed body). a) Raw image b) Pre-processed image using a sliding background subtraction, intensity normalization and a high-pass filter to remove remaining laser reflections. Data processing flow chart shown underneath.

Followed by an intensity normalization and a Gaussian smoothing filter to enhance Gaussian shaped particle intensity distributions. Then cross-correlation was applied on image pairs in multiple passes, starting from an initial interrogation window size of 96×96 pixels with 50% overlap followed by three iterations with a final interrogation window size of 64×64 pixels with 75% overlap, resulting in a spatial resolution of 0.62 mm between adjacent vectors (in-plane). Universal outlier detection (Westerweel and Scarano 2005) was used to detect spurious vectors and remove vectors if the local residual was > 2.0 pixels and reinserting it if the residual was < 3.0 pixels. The filter was applied in regions of 3×3 vectors. Figure 4 shows the particle image before and after pre-processing as well as the whole data processing routine applied on the raw images, underneath.

The subsequent calculation of time-averaged three-dimensional pressure fields based on the scanned stereoscopic PIV data (2D3C) is performed by using the 'Pressure from PIV' software package implemented in Davis 10. The 2D3C vector fields calculated in the previous step are therefore composed in streamwise direction into a 3D volume and finally interpolated. A total number of 20 equidistantly spaced 2D3C-PIV planes is used for the volume interpolation. Within the interpolation process a spatial smoothing filter in spanwise direction was applied over three adjacent planes by using a Gaussian filter kernel within Matlab. Boundary conditions were applied in terms of free-stream velocity and ambient pressure values via a sampling region of ($\Delta y = 30$ mm, $\Delta z = 15$ mm) located at ($x/H = 0.0486$ and $z/H = 1.5$)

3. Results

3.1 Normalized velocity plots

Since the pressure reconstruction in this study is focused on the near wake region behind the Ahmed body, first the flow topology is shown in terms of normalized mean velocity plots extracted 3.5 mm apart the rear surface from PIV data, PTV data and complementary CFD results along three horizontal lines in y - z plane. Figure 5 shows the averaged streamwise mean velocity (in x -Direction) as line plots located at $z/H = 0.208, 0.375$ and 0.542 . The results are normalized by the undisturbed free-stream velocities for both Reynolds number cases, respectively.

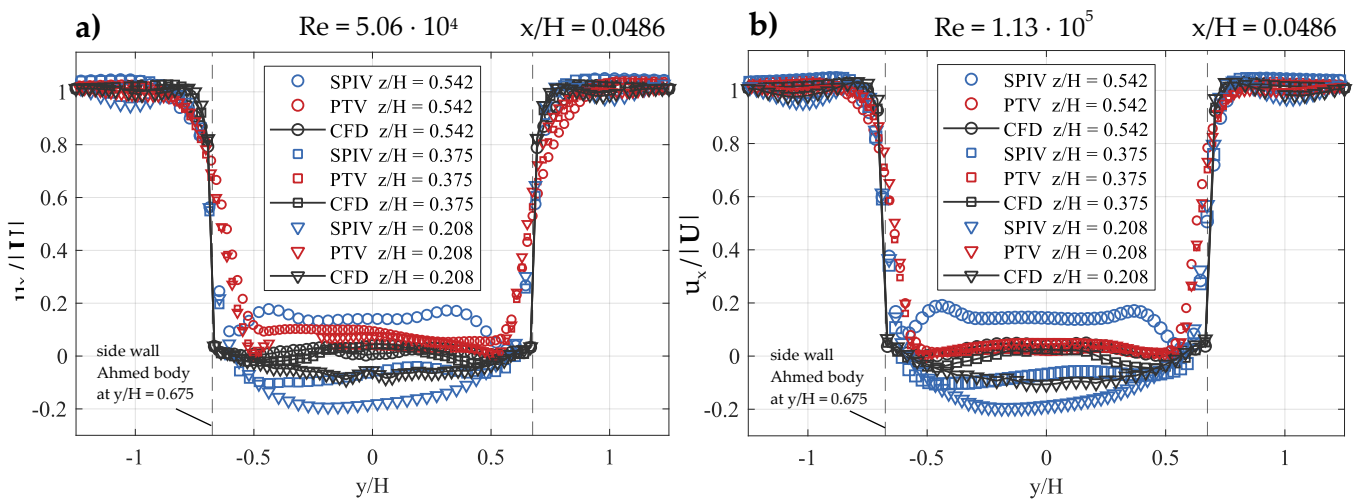


Figure 5: Streamwise velocity profiles extracted at a distance of 3.5 mm behind the pressure tap holes, normalized by the nominal free-stream velocity (a) for the low Reynolds number case $Re = 5.06 \cdot 10^4$ (10ms^{-1}) and (b) for the high Reynolds number case $Re = 1.13 \cdot 10^5$ (23.5ms^{-1}). CFD results based on complementary RANS calculations (not further described in this study).

In general, the velocity plots for both Reynolds number cases show good agreement between PIV- and PTV-based results. However slight differences are clearly visible, e.g. in the transition regions on both sides, between the rear circulation bubble and the outer boundary layers shedding from the side walls, located between $y/H = 0.5$ to $y/H = 0.75$ and $y/H = -0.5$ to $y/H = -0.75$. Furthermore the spatial filtering characteristics of PTV (vector spacing 3.45 mm) and PIV (vector spacing 0.62 mm) apparently leads to an overestimation of the boundary layer thickness and might also be an influencing factor in not fully capturing the recirculatory flow or rather estimating the horizontal and vertical position of the recirculation bubble at slightly different locations, e.g., shown in the PIV-results between $y/H = -0.5$ to $y/H = 0.5$. In addition, figure 6 shows the velocity distributions for both Reynolds numbers in the symmetry plane $y/H = 0$ (figure 6 left column, a), c) and e)) and in spanwise y - z plane at $x/H = 0.0486$ used for pressure extraction (figure 6 right column b), d) and f)).

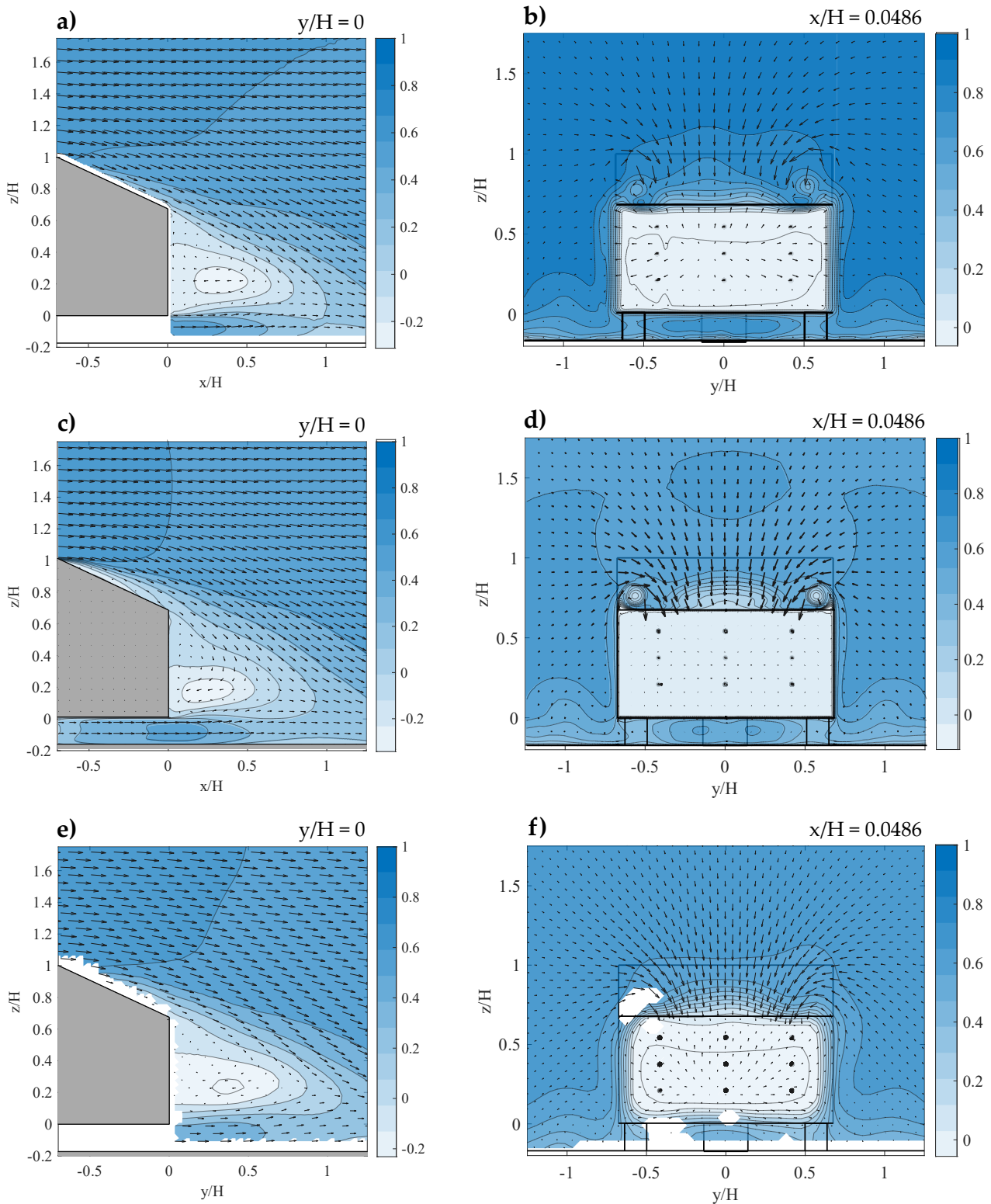


Figure 6: Time-averaged velocity fields normalized by the undisturbed free-stream velocities, for the high Reynolds number case $Re = 1.13 \cdot 10^5$ (10.5 ms^{-1}) a) in streamwise x-y plane; b) spanwise y-z plane located at $x/H = 0.0486$, (3.5 mm behind the rear-surface of the Ahmed body). Only a fraction of vectors is shown for clarity. Stereo-PIV results (top), CFD results (middle) and PTV results (bottom).

Further the convergence of aforementioned velocity fields and their derivatives was analyzed which is plotted in figure 7, exemplary for pressure tab M20. Depending on the number of vector

fields included for ensemble averaging of velocity fields (Fig. 7a), it can be seen that the velocity components are converged to a sufficient extend at 3.000 realizations.

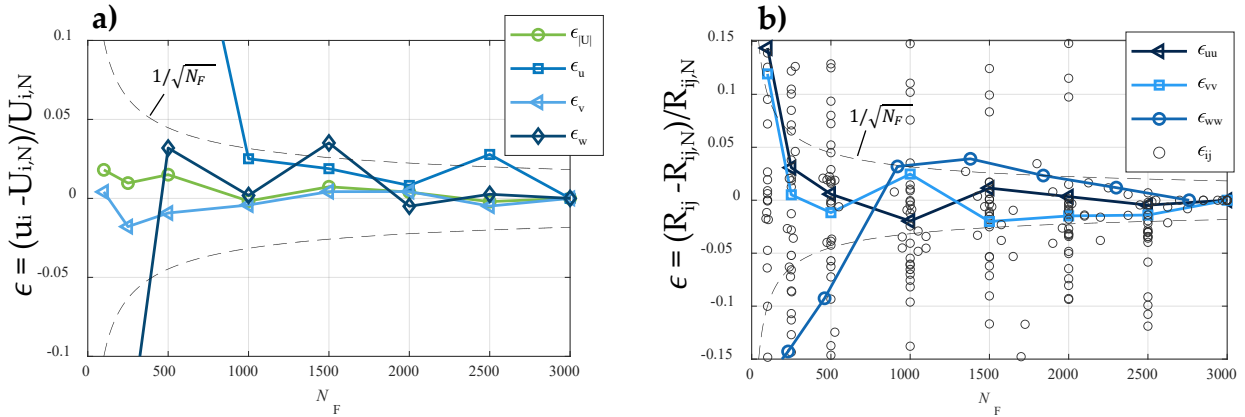


Figure 7: Convergence plots over number of successive stereo-PIV vector fields N_F sampled over pressure tap M20 at $x = 3.5 \text{ mm} = x/H = 0.0486$, $y/H = 0$ and $z/H = 0.375$. a) Convergence of ensemble-averaged velocities as normalized differences to the long-term mean velocities. b) Convergence of ensemble-averaged Reynolds stresses as normalized differences to the long-term average over number of vector fields.

The Reynolds stresses, used for pressure reconstruction, however show a slower convergence rate, as expected, especially the off-diagonal elements (black circles in figure 7 b) are not fully converged even at a number of 3.000 ensembles. Which is believed to promote the error in pressure reconstruction. Table 2 shows the absolute coordinates of the pressure taps based on the reference coordinate system shown in figure 2.

Table 2: Positions of rear-sided surface pressure taps on the Ahmed body

	M19	M20	M21	M38	M39	M40	M44	M45	M46
y [mm]	0	0	0	-30	-30	-30	30	30	30
$y^* = y/H$	0	0	0	-0.42	-0.42	-0.42	0.42	0.42	0.42
z [mm]	39	27	15	39	27	15	39	27	15
$z^* = z/H$	0.54	0.375	0.21	0.54	0.375	0.21	0.54	0.375	0.21

The reconstructed normalized pressure fields based on the ensemble-averaged velocity fields are shown in figure 6 and 7, respectively. The normalized pressure distribution as dimensionless pressure coefficients for both Reynolds number cases are shown, as defined in equation 5.

$$C_{p,i} = \frac{2(\bar{p}_i - \bar{p}_\infty)}{\rho \cdot |\bar{U}_\infty|} \quad \epsilon = \frac{C_{p,i} - C_{p,ref}}{C_{p,ref}} \quad (5)$$

With \bar{p}_i being the ensemble-averaged pressure based on PIV, PTV and CFD velocity data.

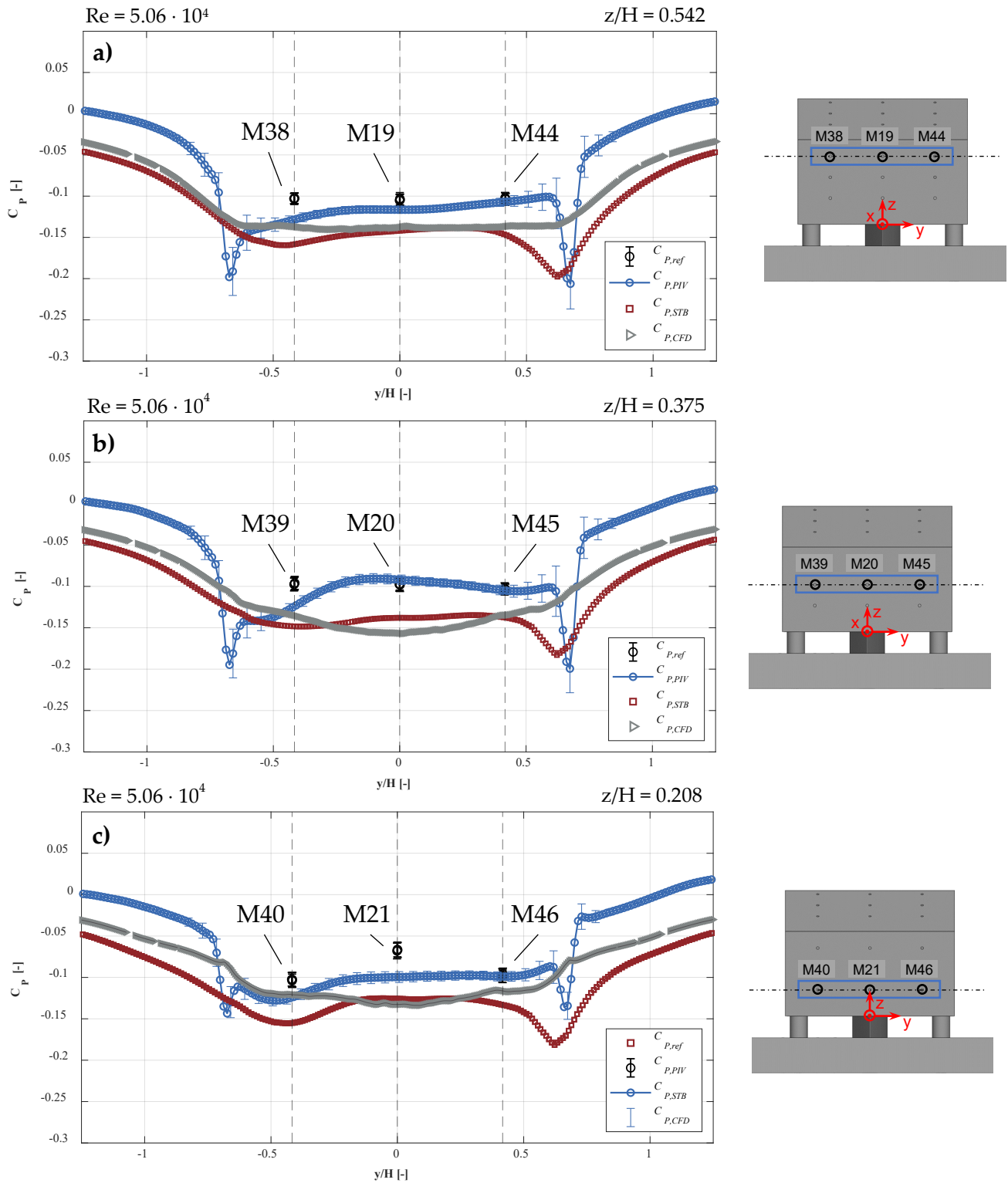


Figure 8: Pressure results for the low Reynolds number case $Re = 5.06 \cdot 10^4$, tap measurements (black) (error bars indicating the 95 % confidence interval), reconstructed pressure data based on Stereo-PIV data (blue) and PTV data (red), measured at 10.5 ms^{-1} free-stream velocity in spanwise y - z plane located at $x = 3.5 \text{ mm}$. Pressure curves are extracted at $z/H = 0.208$ (a), $z/H = 0.376$ (b) and $z/H = 0.542$ (c). RANS-based CFD results are shown additionally (grey).

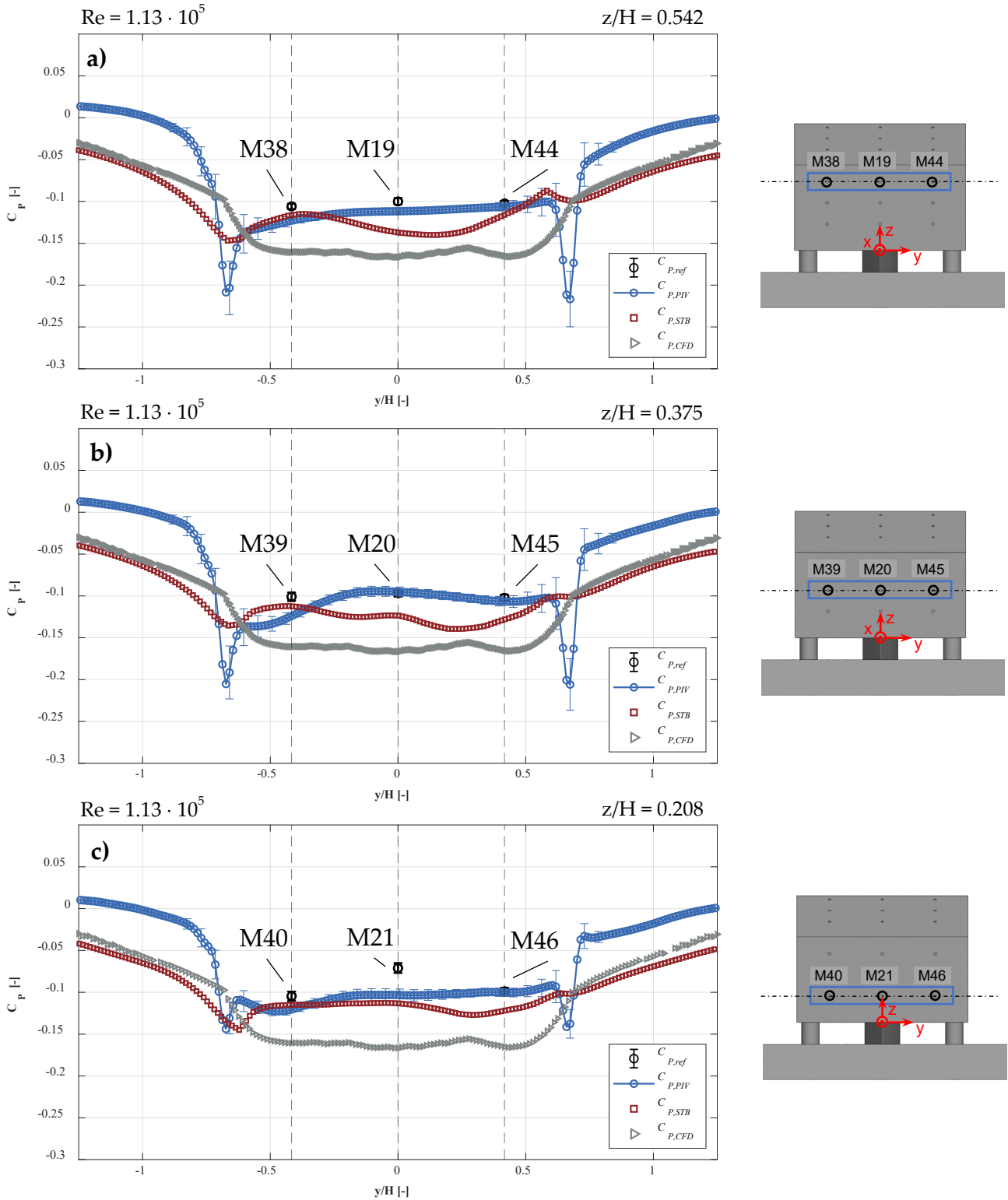


Figure 9: Pressure results for the high Reynolds number case $Re = 1.13 \cdot 10^5$, tap measurements (black) (error bars indicating the 95 % confidence interval) and reconstructed pressure data based on Stereo-PIV data (blue) and PTV data (red), measured at 23.5 ms^{-1} free-stream velocity in spanwise y - z plane located at $x = 3.5 \text{ mm}$. Pressure curves are extracted at $z/H = 0.208$ (a), $z/H = 0.376$ (b) and $z/H = 0.542$ (c). RANS-based CFD results are shown additionally (grey).

Despite a previous study (Ladwig et al. 2023), that focused on the pressure reconstruction in the streamwise symmetry plane, the pressure reconstruction in the wake shows significantly larger deviations between PIV- and PTV-based results compared to pointwise reference pressure data shown in figure 8 and figure 9. Detailed pointwise deviations are listed in table 3 as relative deviations from the reference pressure tap measurements, defined in equation 5. As expected, the pressure results from tap measurements and reconstructed time-averaged PIV-based pressure fields show global agreement, especially in regions where the flow field shows a tendency to be unidirectional, but tends to mismatch in regions where the velocity field appears highly three-dimensional e.g., in detached flow regions and the recirculation bubble, as it is present in the wake flow topology. The results show furthermore that an accurate determination of the near-wall velocity gradients is a necessary basis for a precise determination of the pressure fields. Particularly when surface pressure distributions are to be measured.

Table 3: Deviation between reconstructed pressure coefficients $C_{p,PIV}$, $C_{p,STB}$ and reference pressure coefficients $C_{p,ref}$ for the $Re = 5.06 \cdot 10^4$ (10.5 ms^{-1}) and $Re = 1.13 \cdot 10^5$ (23.5 ms^{-1}) case evaluated at the nine pressure taps M19 – M46 located at the Ahmed body rear surface.

case	pressure taps		Stereo-PIV				Shake-the-Box			
	$C_{p,ref}$ [-]		$C_{p,PIV}$ [-]		ε_{PIV} [%]		$C_{p,STB}$ [-]		ε_{STB} [%]	
	10.5 ms^{-1}	23.5 ms^{-1}	10.5 ms^{-1}	23.5 ms^{-1}	10.5 ms^{-1}	23.5 ms^{-1}	10.5 ms^{-1}	23.5 ms^{-1}	10.5 ms^{-1}	23.5 ms^{-1}
M19	-0.1042	-0.1002	-0.1164	-0.1118	11.7	11.7	-0.1314	-0.1371	26.1	37.1
M20	-0.0977	-0.0967	-0.0920	-0.0951	-5.9	-1.7	-0.1450	-0.1235	48.4	27.7
M21	-0.0671	-0.0711	-0.0996	-0.1033	48.5	45.2	-0.1370	-0.1133	104.3	59.2
M38	-0.1029	-0.1059	-0.1284	-0.1230	24.8	16.1	-0.1465	-0.1164	42.3	9.8
M39	-0.01	-0.1009	-0.1242	-0.1241	28.2	23.0	-0.1553	-0.1124	60.4	11.4
M40	-0.01	-0.1046	-0.1242	-0.1205	-20.5	15.3	-0.1648	-0.1152	60.0	10.2
M44	-0.01	-0.1024	-0.1069	-0.1061	4.0	3.6	-0.1283	-0.1161	24.8	13.3
M45	-0.01	-0.1022	-0.1051	-0.1067	1.9	4.3	-0.1394	-0.1282	35.2	25.4
M46	-0.01	-0.0990	-0.0989	-0.1002	1.6	1.3	-0.1387	-0.1220	42.3	23.3

4 Conclusions

In this contribution time-averaged pressure fields in the near wake of an $\frac{1}{4}$ scaled Ahmed body model are presented. Pressure fields were reconstructed based on time-averaged velocity data acquired by stereoscopic PIV and 3D-PTV (Shake-The-Box) setups. Measurements were conducted under equal conditions in a closed-loop wind tunnel. The results in terms of dimensionless pressure coefficients show qualitatively good agreement between reconstructed PIV- and PTV-based pressure fields and reference pressure measurements using classic wall pressure measurements (see figure 8 + 9). The global characteristics of the pressure distributions are correctly reproduced. The agreement is particularly good in areas of unidirectional flow and locally

smaller velocity gradients. In shear zones and turbulent areas like separation and recirculation areas, larger deviations are clearly visible, as the velocity gradients present near the surface cannot be fully resolved using PIV and PTV in this study, but the global flow character is sufficiently represented overall. Furthermore, the results show that the spatial resolution, as expected, has a direct influence on the velocity field and thus on the calculated velocity gradients and ultimately on the reconstructed pressure field. Since no additional correction scheme was applied on the velocity data, e.g. the divergence correction proposed by Azijki and Dwight (2015) which was further successfully applied by Jacobi et al. (2022), larger differences in the PIV- and PTV-based pressure fields are existent. A further improvement of reconstructed pressure data by means of a a-posteriori divergence correction of PIV/PTV based velocity data, prior to pressure reconstruction, might be promising and will be tested in further work. Nevertheless the reconstruction of time-averaged pressure fields based on PIV/PTV velocity data represents a problem-specific suitable tool for the determination of time-averaged pressure fields within the framework of measurements presented in this study, considering practicability and applicability.

The results, opinions and conclusions expressed in this publication are not necessarily those of Volkswagen Aktiengesellschaft.

Acknowledgments

We would like to thank Alexander Kabat vel Job from Volkswagen AG for performing the CFD calculations and Denis-Karim Küper for his support during the PIV measurements at Bochum University of Applied Sciences.

References

- Adrian, R. J., Westerweel, J. (2011): Particle image velocimetry. Cambridge Univ. Press (Cambridge aerospace series, 30).
- Ahmed, S., Ramm, G., Faltin, G. (1984): Some salient features of the time-averaged ground vehicle wake. SAE Technical Paper 840300,
- Azijli, I., Dwight, R. P. (2015): Solenoidal filtering of volumetric velocity measurements using Gaussian process regression. *Exp. in Fluids* 56 (11).
- Boerger, G. G. (1973): Optimierung von Windkanaldüsen für den Unterschallbereich. Dissertation, Ruhr University Bochum, Bochum.
- De Kat, R., Van Oudheusden, B. W. (2012) Instantaneous planar pressure determination from PIV in turbulent flow. *Exp. in Fluids*, 52(5), 1089-1106.
- De Kat, R., Ganapathisubramani, B. (2012) Pressure from particle image velocimetry for convective flows: a Taylor's hypothesis approach. *Meas. Sci. and Technol.*, 24(2), 024002.

Gericke, T., Erdogdu, A. O., Huettig, S., Ladwig, M., Lindken, R. (2023): Reconstruction of time-averaged 3D pressure fields of an Ahmed body with Pressure from PIV. Part II: Shake-The-Box. 15th International Symposium on Particle Image Velocimetry – ISPIV 2023.

Jacobi, G., Thill, C. H., Huijsmans, R. H. M. (2022): Pressure reconstruction from PIV measurements in the bow region of a fast ship. *Ocean Engineering* 252, S. 110318.

Ladwig, M., Gericke, T., Huettig, S., and Lindken, R. (2023) Reconstruction of time-averaged 3D pressure fields of an Ahmed body with pressure from PIV. Part I: Scanning Stereo-PIV. 15th International Symposium on Particle Image Velocimetry – ISPIV 2023.

Lienhart, H., Becker, S. (2003): Flow and Turbulence Structure in the Wake of a Simplified Car Model. SAE Technical Paper Series. SAE 2003 World Congress & Exhibition.

Jux, C., Scarano, F., and Sciacchitano, A. (2019, July) Aerodynamic pressure reconstruction on generic surfaces from robotic PIV measurements. Proceedings of the 13th International Symposium on Particle Image Velocimetry (pp. 22-27). Universität der Bundeswehr München.

Minguez, M., Pasquetti, R., Serre, E. (2008): High-order large-eddy simulation of flow over the “Ahmed body” car model. *Physics of Fluids* 20 (9), S. 95101.

Prasad, A. K. (2000): Stereoscopic particle image velocimetry. In: *Exp. in Fluids* 29 (2), S. 103–116.

Schanz, D., Gesemann, S. and Schröder, A. (2016) Shake-The-Box: Lagrangian particle tracking at high particle image densities. *Exp. in Fluids*, 57(5), 1–27

Sellappan, P., McNally, J., Alvi, F. S. (2018): Time-averaged three-dimensional flow topology in the wake of a simplified car model using volumetric PIV. *Exp. in Fluids* 59 (8).

van Gent, P. L., Michaelis, D., Van Oudheusden, B. W., Weiss, P. É., de Kat, R., Laskari, A., and Schrijer, F. F. J. (2017) Comparative assessment of pressure field reconstructions from particle image velocimetry measurements and Lagrangian particle tracking. *Exp. in Fluids*, 58(4), 33.

van Oudheusden, B. W., Scarano, F., Roosenboom, E. W. M., Casimiri, E. W. F., Soverein, L. J. (2007): Evaluation of integral forces and pressure fields from planar velocimetry data for incompressible and compressible flows. *Exp. in Fluids* 43 (2-3), S. 153–162.

van Oudheusden, B. W. (2013): PIV-based pressure measurement. *Meas. Sci. Technol.* 24 (3), S. 32001.

Westerweel, J., van Oord, J. (2000): Stereoscopic PIV measurements in a turbulent boundary layer. In Stanislas M., Kompenhans J., & Westerweel J. (Eds.), *Particle image velocimetry: Progress towards industrial application* (pp. 459-478). Kluwer.

Westerweel, J., Scarano, F. (2005): Universal outlier detection for PIV data. *Exp. in Fluids* 39 (6), S. 1096–1100.

Wieneke, B. (2005): Stereo-PIV using self-calibration on particle images. *Exp. in Fluids* 39 (2), S. 267–280.

Willert, C. (1997): Stereoscopic digital particle image velocimetry for application in wind tunnel flows. *Meas. Sci. Technol.* 8 (12), S. 1465–1479.